

# Fault Localization and Ranging Method for Multi-Branch Collector Lines in Wind Farms Based on the Improved PSO-VMD-TEO Traveling Wave Extraction

Li-Ying Zhao<sup>1</sup>, Si-Nan Shi<sup>2\*</sup>, En-Tie Qi<sup>3</sup>,  
Jin Zhu<sup>2</sup>, and Yu Wang<sup>2</sup>

<sup>1</sup> School of Computer Technology and Engineering, Changchun Institute of Technology,  
Changchun 130012, China  
zhaoly415@ccit.edu.cn

<sup>2</sup> School of Electrical and Information Engineering, Changchun Institute of Technology,  
Changchun 130012, China  
{shisinan, zhujin, wangyu}@stu.ccit.edu.cn

<sup>3</sup> Modern Education Technology Center, Changchun Institute of Technology,  
Changchun 130012, China  
qientie@ccit.edu.cn

*Received 26 May 2025; Revised 2 June 2025; Accepted 2 June 2025*

**Abstract.** The paper presents a multi-branch collector line segment localization and fault ranging method based on the improved PSO-VMD-TEO traveling wave extraction. Before the fault occurs, the inherent distance difference matrix of the collector line is established based on the traveling wave propagation characteristics and the collector line topology. After the fault occurs, the initial parameter settings of Variational Mode Decomposition (VMD) are optimized using Particle Swarm Optimization (PSO) to decompose the initial fault traveling wave signals into multiple Intrinsic Mode Function (IMF) signals. The improved TEO energy operator is used to assess the distance between the faults, analyze the first IMF signal, and determine the time when the initial wavehead reaches the measurement point. The double-ended traveling wave ranging method establishes the fault distance difference matrix. Through the difference between IDM and FDM, the fault section discrimination matrix of the multi-branch collector line is constructed, and accurate distance measurement of collector line faults is completed according to the discriminated fault sections. The simulation results of PSCAD/EMTDC prove that the proposed method accurately measures the fault distance based on the fault section localization, being unaffected by the fault types, transition resistances, and noise interferences.

**Keywords:** collector line, multi-branch fault location, traveling wave ranging, variational modal decomposition, particle swarm algorithm

## 1 Introduction

Wind power is characterized by abundant green non-pollution sources, providing a vital contribution to transforming the global energy structure [1, 2]. The terrain of wind farms in China is mainly located in the Gobi desert, grasslands, coasts, and hills, which have strong winds but relatively harsh climatic and geographic environments. Some areas with serious dust pollution or humid air face frequent fails of collector lines used to collect wind turbine power in wind farms, yielding huge economic losses instead of expected gains [3]. On the other hand, the intricate topology of wind farm collector systems poses significant challenges for manual fault inspection. The complex network architecture often impedes rapid fault localization during line failures, where delayed identification of fault positions may lead to substantial wind power curtailment. Consequently, developing an effective fault location methodology for multi-branch collector systems becomes crucial for timely fault clearance, thereby enhancing operational efficiency, minimizing energy losses in wind farm operations faults in time, and reducing the operating costs of wind farms.

The available fault location techniques on collector lines mainly comprise fault analysis method [4, 5], travel-

ing wave method [6, 7], and artificial intelligence method [8, 9]. The fault analysis method determines the fault point based on the circuit principle, according to the voltage and current collected from single or multiple ends of the line. Based on the existing differential equation ranging formula, Li and Zheng [10] establish the relationship equation between the amount of voltage and current change at the protection installation point and the voltage at the fault point in the frequency domain, which accurately compensates the error caused by the phase inconsistency, and convert the equation to the time domain and solve it by continuous sampling and integration using the R-L model, which improves the ranging accuracy and speed. Cheng and Li [11] considered that the positive and negative sequence impedance angles on both sides of the fault point should be assumed equal and accomplished fault localization by the shunt coefficient and line fault component. The assumptions of the above studies all default to the same phase of the fault components at both ends of the fault point, which can certainly improve the localization accuracy to a certain extent but is greatly affected by the system impedance angle of the fault point. Li and Sun [12] proposed a new type of zero-sequence current-based collector line asymmetrical grounding fault localization scheme, which realized the section localization of the collector line by constructing an information network matrix using the main flow path of zero-sequence current. However, only single-phase and two-phase short-circuit faults have the zero-mode component, in contrast to three-or four-phase ones. So, realizing multi-phase fault segments' positioning in collector lines is impossible.

The traveling wave method calculates the fault location from the relationship between propagation time and wave speed by identifying the transient traveling wave generated after a line fault. Applying the traveling wave method for fault location requires the extraction of the fault traveling wave components (current or voltage), determining wave speed, and calibrating the wave reaching time. Zhang and Song [13] employed wavelet transform to analyze non-smoothly fluctuating transient traveling wave signals, demonstrating effective time-frequency analysis and noise cancellation to extract fault traveling waves from voltage or current data for fault localization in transmission lines. Nevertheless, the wavelet transform necessitates careful selection of the wavelet basis function and decomposition size; improper selection of these parameters significantly affects fault localization. Oliveira and Moreira [14] introduced the Empirical Mode Decomposition (EMD) in the Heber-Huang transform to extract fault traveling wave signals, which overcomes the difficult problem of selecting the basis function and decomposition scale in the wavelet transform. However, EMD suffers from mode aliasing, over-envelopment, and under-envelopment problems when performing signal decomposition. Alternatively, Xie and Li [15] addressed the resolution of modal aliasing in EMD decomposition and used the Teager energy operator instead of the Hilbert transform and wavehead identification, which effectively responded to the signal amplitude and frequency transforms and better detected the detection of signal singularities. Wu and Qiu [16] comprehensively combined VMD with the wavehead signal method approach, encapsulating the signal's ephemeral singularity and significantly improving modal decomposition's stability. However, the decomposition effect of VMD was strongly affected by the human factor.

The artificial intelligence method has excellent feature extraction capability, which can deeply mine the relevant information on fault location in the fault samples [17-21]. In particular, Yang and Wang [19] collected fault voltage and current from the distribution network and derived the corresponding positive, negative, and zero sequence components, negative and zero sequence components, used them to construct the feature volume image of the three sequence components, and applied the migration learning technique to complete the model training, localizing the transmission line grounding fault. Alternatively, Peng and Wang [20] aggregated the voltage and current phase measurements at the initial end of the line to create a data set. They utilized the limit gradient boosting method and long short-term memory neural network to develop a regression model for determining collector line fault location, thus avoiding the complex wind turbine-containing fault analysis process. Meng and Du [21] determined the fault section by comparing the zero sequence current waveforms at both ends, constructing a regression model with the voltage and current phasors at both ends, and calculating the fault location. However, the algorithm's performance and the richness or otherwise of the fault information contained in the inputs will impact the AI scheme's localization effect, so the selection of the algorithm type and the inputs need to be further studied.

Aiming at the abovementioned problems, this paper presents a multi-branch collector line fault localization method. This method combines the improved wavehead detection algorithm with the fault section discriminant matrix (FSIM) to accomplish multi-branch collector line section localization and fault ranging. The key contributions of this research are delineated as follows.

1. A new fault ranging method based on improved VMD-TEO is proposed. The improved VMD method can accurately identify the faulty traveling waveheads under noise interference and effectively identify the arrival time of the waveheads, showing strong anti-interference effects. In addition, the application of the improved VMD algorithm solves the problems of data accuracy loss and modal aliasing problems that occur when the tra-

ditional VMD algorithm's mode parameters are not selected properly.

2. A multi-branch fault localization method applied to collector lines is introduced. Based on the wind farm topology, the intrinsic distance difference matrix is established; based on the double-ended traveling wave method, the fault distance difference matrix is obtained, and the fault zone discrimination matrix is established according to the difference between it and the intrinsic distance difference matrix. The elemental characteristics of the discriminant matrix are analyzed when different zones are faulty, and the fault zone localization is realized. Based on segment localization, the precise positioning of the collector line is accomplished by the double-end localization method.

The rest of this paper is structured as follows: section 2 describes a new fault traveling wave detection method. Section 3 presents a multi-branch fault localization method for collector lines. Section 4 provides simulation verification, and Section 5 concludes the paper.

## 2 Collector Line Fault Traveling Wave Detection Method

The wind turbine incorporates numerous power electronic devices and has a doubly-fed control technique. In the event of a fault in a wind farm collector line, characteristics such as diminished feedthrough, main frequency deviation, and elevated harmonic content are observed. The primary frequency of the detected fault current may shift by 50Hz, and both the fault voltage and current exhibit a significant presence of high harmonic components; the traditional traveling wave ranging methods are inadequate for determining the fault location within the wind farm collector line. Therefore, this paper combines the PSO-optimized VMD with the improved TEO algorithm to accurately detect fault traveling waveheads under high harmonics and strong noise interference.

### 2.1 The Basic Principles of VMD

VMD is an innovative and entirely non-recursive approach to modal variability. VMD can handle nonlinear and nonsmooth signals well, demonstrating exceptional noise resilience while preserving efficient information extraction capabilities despite substantial noise interference.

The VMD systematically seeks the optimal solution of the model by the alternating direction multiplier approach, which disaggregates a complex signal into several intrinsic modal components (IMFs), where the  $k$ th IMF is denoted as  $u_k(t)$ , and the bandwidth of each IMF represents a specific frequency component of the signal. The following steps were performed to calculate the bandwidth:

1. The one-sided spectrum of the determined signal of each IMF was solved using the Hilbert transform, and the resolved signal of each IMF was mixed with the signal at the predicted center frequency. The bandwidth of each modal signal was assessed based on the  $L^2$  norm of the gradient of the demodulated signal, with the expression of the variational problem with constraints as in Eq. (1).

$$\begin{cases} \min_{\{u_k\}, \{\omega_k\}} \left\{ \sum_k \left\| \left[ \delta(t) + \frac{j}{\pi t} \right] * u_k(t) e^{-j\omega_k t} \right\|_2^2 \right\} \\ s.t. \sum_k u_k = f(t) \end{cases} \quad (1)$$

where  $\{u_k\}$  is the  $k$ -th IMF component;  $\{e^{-j\omega_k t}\}$  is the anticipated central frequency of the modal component, and  $f(t)$  is the fault traveling wave signal.

2. The quadratic penalty factor  $\alpha$  and the Lagrangian coefficient  $\lambda(t)$  were introduced when solving the variational problem. The quadratic penalty factor  $\alpha$  achieved high fidelity in the signal reconstruction process and is more suppressive to Gaussian noise. The two cooperated to solve the constraint problem in Eq. (1) and obtain the augmented Lagrangian expression:

$$L(\{u_k\}, \{\omega_k\}, \lambda(t)) = \alpha \sum_k \left\| \partial_t \left[ \left( \delta(t) + \frac{j}{\pi t} \right) u_k(t) \right] e^{-j\omega_k t} \right\|_2^2 + \left\| f(t) - \sum_k u_k \right\|_2^2 + \langle \lambda(t), f(t) - \sum_k u_k \rangle. \quad (2)$$

By solving the augmented Lagrangian function via Eq. (2), alternating direction multipliers and alternating update iterations  $\omega_k^{n+1}, u_k^{n+1}, \lambda_k^{n+1}$ , the issue of determining the minimum of Eq. (1) was reformulated as a saddle point problem involving the augmented Lagrangian, resulting in the formulas for each modal component and center frequency as delineated in Eqs. (3) and (4):

$$\vec{u}_k^{n+1}(\omega) = \frac{\vec{f}(\omega) - \sum_{i < k} \vec{u}_i^{n+1}(\omega) - \sum_{i > k} \vec{u}_i^n(\omega) + \frac{\vec{\lambda}(\omega)}{2}}{1 + 2\alpha(\omega - \omega_k^n)^2} \quad (3)$$

$$\omega_k^{n+1} = \frac{\int_0^\infty \omega |\vec{u}_k^{n+1}(\omega)|^2 d\omega}{\int_0^\infty |\vec{u}_k^{n+1}(\omega)|^2 d\omega} \quad (4)$$

where VMD decomposition was realized by setting the quadratic penalty factor  $\alpha$  and the center angle frequency initialization to obtain the center angle frequency  $\omega_k$ ; then, the eigenmode function  $u_k$ , the modes, and the center frequency were continuously updated cyclically to attain the adaptive optimal decomposition of the signal.

## 2.2 Maintaining the Integrity of the Specifications

The VMD decomposition algorithm focuses on determining the number of modal decompositions  $K$  and the penalty factor  $\alpha$ . An excessively large or small values of  $K$  may result in over-decomposition or signal loss modal aliasing, respectively. To solve the problem of poor signal decomposition and uncertainty of decomposition effect when the parameters were set artificially in VMD decomposition, the PSO algorithm was used in this paper to optimize the VMD decomposition and determine the optimal  $K$  and  $\alpha$  in the VMD algorithm.

Particle Swarm Optimization (PSO) is an adaptive optimization technique that parallels the search for food with the optimal solution set of an optimization problem, emulating the foraging behavior of birds in nature and the velocity and position of birds with those of massless particles. Each particle independently searches for the optimal solution and is recorded as an individual optimal solution. The global optimal solution (*gbest*) is generated from the mutual sharing of local optimal solutions (*pbest*), and the particle updates its velocity and location for the  $t + 1$ st displacement via Eq. (5):

$$\begin{cases} v_i^{t+1} = \omega \cdot v_i^t + c_1 r_1 (p_i^t - x_i^t) + c_2 r_2 (g_i^t - x_i^t) \\ x_i^{t+1} = x_i^t + v_i^{t+1} \end{cases} \quad (5)$$

where  $\omega$  represents the inertia weight factor,  $c_1$  and  $c_2$  denote the learning factors, while  $r_1$  and  $r_2$  are random values within the interval  $\{0, 1\}$ ;  $p_i^t$  and  $g_i^t$  denote the local history optimal solution and global history optimal solution, respectively;  $x_i^t$  and  $v_i^t$  denote the particle's flight velocity and position vectors in  $t$  evolutionary generations.  $x_i^t$  and  $v_i^t$  satisfy Eq. (6), as follows:

$$\begin{cases} x_i \in [x_{min}, x_{max}] \\ v_i \in [v_{min}, v_{max}] \\ v_{max} = \gamma x_{max} \end{cases} \quad (6)$$

where  $\gamma$  is the coefficient of proportionality between the maximum velocity  $v_{max}$  of the particle and the maximum search space  $x_{max}$ .

The PSO fitness function was the magnitude of the envelope entropy, indicating the signal's periodic characteristics: a higher entropy value signifies diminished periodicity and increased complexity, and vice versa. Envelope entropy is defined by Eq. (7):

$$\begin{cases} E_k = -\sum_{j=1}^N p_{k,j} \log_{10} p_{k,j} \\ p_{k,j} = a_k(j) / \sum_{j=1}^N a_k(j) \end{cases} \quad (7)$$

where  $k$  is the number of decomposition layers in the VMD;  $p_{k,j}$  is the normalized representation of  $a_k(j)$ ;  $a_k(j)$  signifies the envelope signal of the modal signal decomposed by the VMD after the Hilbert transforms.

The PSO algorithm utilized envelope entropy as the optimization objective to determine the number of decomposition layers  $K$  and the penalty factor  $\alpha$ , hence achieving optimal parameter selection in the VMD decomposition process. The optimization procedure of VMD with PSO contained the following steps (see Fig. 1):

(1) PSO parameters' initialization. Establish the initial parameters of the PSO method, compute the initialization fitness value, where  $M$  is the population size, and  $G_{\max}$  is the maximum number of iterations for the population.

(2) Particle swarm initialization. Randomly establish the particle swarm's beginning position and each particle's velocity.

(3) Assessment of termination criteria. Compute the fitness value VMD for each particle position, evaluate the magnitude of the fitness values, and determine whether the output represents the best settings.

(4) Determining the best possible combination of parameters  $\alpha$  and  $K$ . After each iteration, update the particle positions and velocities to see how they change in terms of fitness. Based on these changes, decide whether to continue looping until the maximum number of iterations is reached or the optimal combination of parameters is found.

(5) VMD decomposition. The acquired set of optimal parameter combinations  $[\alpha, K]$  is set as the initial parameters of VMD, and signal decomposition is performed to obtain each IMF component.

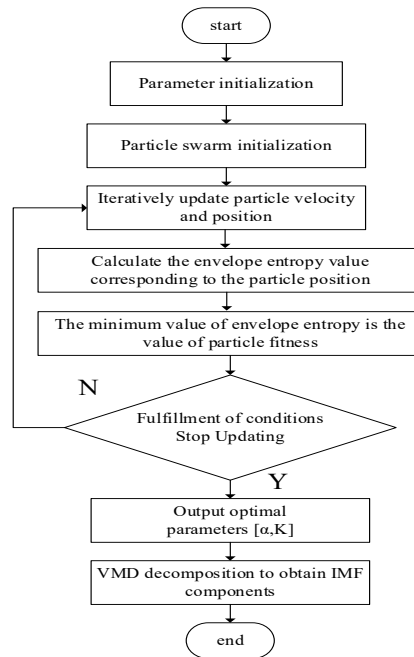


Fig. 1. PSO-based optimization of the VMD process

### 2.3 Maintaining the Integrity of the Specifications

The PSO-optimized VMD algorithm can realize the collector line fault signal decomposition, which is more stable and can respond well to the signal transient singularity characteristics compared with the traditional signal decomposition algorithms, empirical modal decomposition (EMD), local mean decomposition (LMD), and ensemble empirical modal decomposition (EEMD). It has a high anti-noise and anti-interference ability when dealing with collector line signals with high harmonics, frequency offsets, and high noise.

The Teager Energy Operator (TEO) is a nonlinear operator capable of effectively extracting the energy from a signal, reflecting the instantaneous energy change, and is widely used in traveling wave ranging. The TEO is defined for a discrete signal  $x(n)$  as follows:

$$\psi(x(n)) = x^2(n) - x(n-1)x(n+1). \quad (8)$$

where  $\psi(x(n))$  is the high-frequency energy operator of the original signal  $x(n)$ .

To improve the processing capability of the conventional TEO at higher-order frequencies. The TEO discrete signal  $x(n)$  is rewritten as an  $N$ -th-order derivative via Eq. (9), and its parameters are introduced into the high-order frequency energy operator, the expression of the improved TEO:

$$\varphi(x(n)) = x^m(n) - x^{m-1}(n)x(n) - \dots - x(n-1)x^{m-1}(n+1). \quad (9)$$

$$\zeta(x(n)) = x^m(n) - x^{m-1}(n-i)x(n+i) - \dots - x(n-i)x^{m-1}(n+i). \quad (10)$$

where  $\varphi(x(n))$  is the high-frequency energy operator of the initial signal  $x(t)$ ;  $\zeta(x(n))$  is the new high-frequency energy operator of the original signal; and  $m$  is the  $m$ -th-order derivative.

Equation (10) implies that the enhanced TEO employs the values of adjacent  $i$  sampling points to synthesize the response signal's instantaneous energy, significantly mitigating the impact of high-frequency noise on wave-head extraction accuracy.

The enhanced TEO energy operator effectively extracts the amplitude and frequency of single-component high-frequency transient events. This work integrates the benefits of PSO-VMD and enhanced TEO to achieve the calibration of the traveling wavehead for multi-branch collector line faults.

The precise steps are outlined in Fig. 2.

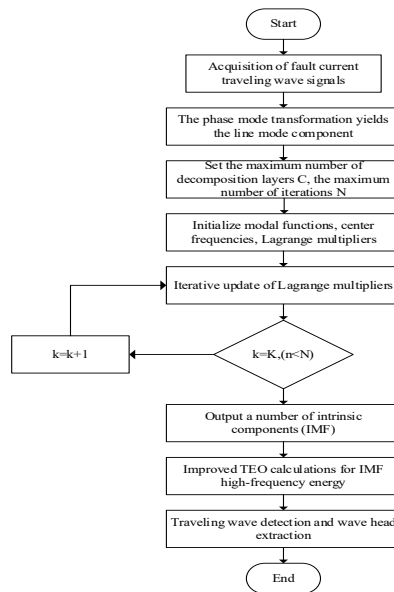


Fig. 2. Flowchart of faulty wavehead extraction with improved PSO-VMD-TEO

The particular steps were as follows:

- (1) Determine and read the fault voltage traveling wave  $U_L$  monitored at each line's endpoint after a fault occurs on the collector line.
- (2) Decouple the three-phase coupled fault voltage traveling wave using the Karenbauer phase-mode transform to obtain the  $U_\alpha$  fault voltage traveling wave's line mode component.
- (3) Optimize the VMD's dynamic parameters using the PSO optimization algorithm. After determining the optimal  $k$  and  $\alpha$  values, and decompose  $U_\alpha$  using the VMD.
- (4) Select the modal component with the maximum craggy value and calibrate the moment the initial wave-head  $U_\alpha$  reaches the line measurement endpoint using the improved TEO energy operator.

### 3 Fault Section Localization and Ranging Method for Multi-branch Collector Lines

Aiming at the characteristics of wind farm collector lines branching multiple power sources and mixed lines, this paper proposes to use the construction of a multi-branch fault section discrimination matrix to complete the section positioning of multi-branch fault lines, on this basis combined with the wave speed of the equivalent mixed lines and double-ended traveling wave positioning method, to complete the precise positioning of multi-branch fault lines.

#### 3.1 Multi-branch Fault Section Identification Based on Distance Matrix

The power line system adopted a chain structure, with multiple WTGs connected to each main collector line. Fig. 3 shows a typical wind turbine chain structure, where  $M_1$  is the substation endpoint,  $M_{n-2}$  is the wind turbine endpoint, and  $T_i$  is the branch node. Fault traveling wave collection devices are installed on both the substation and units.

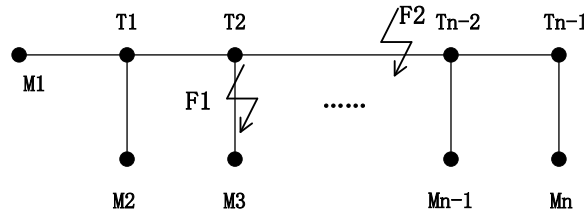


Fig. 3. Multi-branch collector line structure

Since the collector line topology is known (both the distance between  $M_i$  and  $T_i$ ), the intrinsic distance difference matrix (IDM) of each endpoint  $M_i$  with the neighboring node  $T_i$  as a reference is computed via Eq. (11):

$$L_{Mij} = L_{MIT} - L_{MjT} \tag{11}$$

where  $L_{MIT}$  and  $L_{MjT}$  are the distances from the line endpoints  $M_i, M_j$  to the reference node  $T$ . This yields:

$$L = \begin{bmatrix} 0 & L_{M12} & L_{M13} & \cdots & L_{M1(n-1)} & L_{M1n} \\ L_{M21} & 0 & L_{M23} & \cdots & L_{M2(n-1)} & L_{M2n} \\ L_{M31} & L_{M32} & 0 & \cdots & L_{M3(n-1)} & L_{M3n} \\ \vdots & \vdots & \vdots & \ddots & \cdots & \cdots \\ L_{M(n-1)1} & L_{M(n-1)2} & L_{M(n-1)3} & \cdots & 0 & L_{M(n-1)n} \\ L_{Mn1} & L_{Mn2} & L_{Mn3} & \cdots & L_{Mn(n-1)} & 0 \end{bmatrix} \tag{12}$$

When a fault occurs at point  $F$  at any location of the line, by improving the PSO-VMD-TEO to calculate the time of traveling wave to each endpoint, then the distance from endpoints  $M_1 \sim M_n$  to the fault point  $F$  can be determined using the double-ended traveling wave ranging equation (13).

$$\begin{cases} d_{M_i F} = \frac{(t_{M_i F} - t_{M_j F}) \times v + d_{M_i M_j}}{2} \\ d_{M_j F} = \frac{(t_{M_j F} - t_{M_i F}) \times v + d_{M_i M_j}}{2} \end{cases} \quad (13)$$

where  $t_{M_i F}$  and  $t_{M_j F}$  are the times when a faulty traveling waves are identified at the endpoints  $M_i$  and  $M_j$ , respectively;  $v$  represents the propagation velocity of the faulty traveling wave along the route. Then, the distances  $d_{M_i F}$  and  $d_{M_j F}$  between the endpoints and the fault point  $F$  are derived, and the difference of the fault distance of each endpoint,  $D_{M_{ij}}$ , is calculated via Eq. (14):

$$D_{M_{ij}} = d_{M_i F} - d_{M_j F} \quad (14)$$

where  $d_{M_i F}$  and  $d_{M_j F}$  are the distances from the line endpoints  $M_j, M_i$  to the fault point  $F$ .

The fault distance matrix (FDM) was constructed as follows:

$$D = \begin{bmatrix} 0 & D_{M_{12}} & D_{M_{13}} & \cdots & D_{M_{1(n-1)}} & D_{M_{1n}} \\ D_{M_{21}} & 0 & D_{M_{23}} & \cdots & D_{M_{2(n-1)}} & D_{M_{2n}} \\ D_{M_{31}} & D_{M_{32}} & 0 & \cdots & D_{M_{3(n-1)}} & D_{M_{3n}} \\ \vdots & \vdots & \vdots & \ddots & \cdots & \cdots \\ D_{M_{(n-1)1}} & D_{M_{(n-1)2}} & D_{M_{(n-1)3}} & \cdots & 0 & D_{M_{(n-1)n}} \\ D_{M_{n1}} & D_{M_{n2}} & D_{M_{n3}} & \cdots & D_{M_{n(n-1)}} & 0 \end{bmatrix} \quad (15)$$

Finally, the fault section identification matrix (FSIM) of the collector line  $\delta$  was established through the constructed intrinsic distance difference matrix  $L$  and fault distance difference matrix  $D$  as follows:

$$\delta = D - L \quad (16)$$

When a fault  $F_1$  occurs on a line branch  $M_i T_j$  ( $M_3 T_2$  in Fig. 3), Eq. (17) holds for the fault section discrimination matrix  $\delta$  of the collector line as follows:

$$\delta = \begin{bmatrix} 0 & 0 & 2(L_{r_{1T_2}} + L_{r_{3F}}) & \cdots & L_{T_n-4T_n-2} + 2L_{T_n-2M_n-1} & 2L_{T_n-4T_n-2} + 2L_{T_n-1M_n} \\ 0 & 0 & 2(L_{r_{1T_2}} + L_{r_{3F}}) & \cdots & 2L_{T_n-4T_n-2} & 2L_{r_{2T_5}} \\ -2(L_{r_{1T_2}} + L_{r_{3F}}) & -2(L_{r_{2T_3}} + L_{r_{2F}}) & 0 & \cdots & -2L_{T_n-4F} & -2L_{r_{2F}} \\ \vdots & \vdots & \vdots & \ddots & \cdots & \cdots \\ -2L_{T_n-2T_n-1} & -2L_{r_{2T_3}} & 2L_{T_n-4F} & \cdots & 0 & 0 \\ -2L_{T_n-1T_n} & -2L_{r_{2T_3}} & 2L_{T_n-4F} & \cdots & 0 & 0 \end{bmatrix} \quad (17)$$

From the values of the elements of the matrix expression (17), it can be seen that the row elements of the M3 end do not exceed zero, while the column elements of the M3 end have less than zero values. The row and column elements of the other endpoints do not have the same pattern. So, M1 is chosen as the reference end to esti-

mate the fault distance. It is introduced that when the fault occurs in  $M_i T_j$  none of the  $M_i$  endpoint elements in the fault zone discrimination matrix  $\delta$  is greater than 0 and none of the column elements is less than 0, both:

$$\begin{cases} \delta(:, i)_{\min} \geq 0 \\ \delta(i, :)_{\max} \leq 0 \end{cases}, i \in (1, 2, \dots, n). \quad (18)$$

where  $\delta(:, i)_{\min}$  and  $\delta(i, :)_{\max} \leq 0$  are the minimum and maximum values of all elements in the  $i$ -th column and  $j$ -th row, respectively.

When the fault occurs at any two neighboring reference nodes  $T_i T_j$ , referring to Fig. 3, the fault occurs on F2 of the line branch T3T4. Similarly, the expression (19) for the fault segment discriminant matrix  $\delta$  is constructed.

$$\delta = \begin{bmatrix} 0 & 0 & 2L_{F1F2} & 2L_{F1F2} & L_{F1F4} + L_{F2F4} & \dots & L_{F1Tn-1} + L_{Tn-2Tn-1} \\ 0 & 0 & 2L_{F1F3} & 2L_{F1F2} & 2L_{F1F3} + L_{F3F4} & \dots & L_{F1Tn-2} + L_{Tn-2Tn-1} \\ -2L_{F1F2} & -2L_{F1F3} & 0 & 0 & -L_{F4F5} & \dots & -L_{Tn-4Tn-1} \\ 0 & 0 & 0 & 0 & L_{F3F4} & \dots & L_{Tn-4Tn-1} \\ \vdots & \vdots & \vdots & \vdots & \vdots & \dots & \vdots \\ -L_{F1Tn-2} & -L_{Tn-4Tn-2} & -2L_{F1Tn-3} & -L_{Tn-3Tn-2} & -2L_{Tn-4Tn-2} & -L_{F3F4} & -L_{Tn-3Tn-2} & 0 & \dots & 0 \\ -L_{F1Tn-1} & -L_{Tn-2Tn-1} & -L_{F1Tn-2} & -L_{Tn-4Tn-2} & -L_{Tn-4Tn-1} & -L_{Tn-2Tn-1} & 0 & 0 & 0 & 0 \end{bmatrix}. \quad (19)$$

From the values of the elements of the matrix expression (19), it can be seen that the dot product of the row elements of M4 (T3 reference node) with those of M5 (T4 reference node) is equal to 0. It follows from this that the dot product of the row elements of  $M_i$  with those of  $M_j$  in the adjudication matrix  $\delta$  is 0, both:

$$\delta(i, :)_{\max} * \delta(:, j)_{\min} = 0 \quad i, j \in (1, 2, \dots, n). \quad (20)$$

Where  $\delta(:, j)_{\min}$  is the minimum value among all elements in the  $j$ -th column;  $\delta(i, :)_{\max}$  is the maximum value among all elements in the  $i$ -th row.

### 3.2 Precise Localization Based on Double-ended Traveling Waves

Wind farm collector lines contain cables and overhead lines. Because of the substantial disparity in the propagation speeds of traveling waves in these media, normalization of the traveling wave speeds is necessary. In this paper, the equivalent wave speed method is used, and the traveling wave flowing from the fault point to the measurement point is the line mode component  $v_x$ , and the traveling wave speed is divided into the cable wave speed

$v_1 = \frac{1}{\sqrt{L_1 C_1}}$ , the overhead line wave speed  $v_2 = \frac{1}{\sqrt{L_2 C_2}}$ , and the equivalent wave speed is taken as equation (21).

$$v_x = \frac{2v_1 v_2}{v_1 + v_2}. \quad (21)$$

According to the above analysis, the multi-branch fault localization of the collector line needs to be accurate at the moment when the initial traveling wave of the fault reaches each endpoint, the fault branch judgment matrix must be established, and the collector segment localization must be completed. After obtaining the fault section of the collector line, the adjacent endpoints of the fault section are used to judge the fault distance from the fault point to the neighboring endpoints by combining the double-ended traveling wave method to complete the accu-

rate positioning of the collector line. To reduce the influence of various factors on the matrix elements, resulting in the possible deviation of the judgment matrix  $\delta$ , which leads to the zero element not being 0, it is necessary to adjust the value of the matrix elements using the error margin  $\mu$ , which is taken to be  $-100m \leq \mu \leq 100m$ . The fault localization process is shown in Fig. 4.

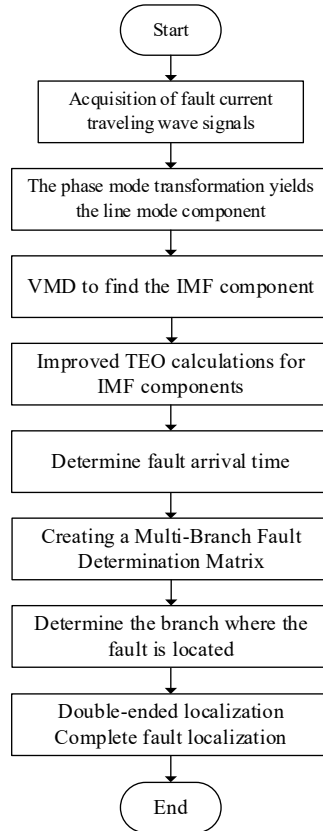


Fig. 4. Multi-branch collector line fault localization method

## 4 Simulation Verification

To verify the efficacy and dependability of the proposed multi-branch fault localization technique for collector lines, this paper combines the actual parameters of wind turbines, transformers, collector lines, and traveling wave collection devices of a wind farm with a wind farm collector line model constructed using electromagnetic transient PSCAD/EMTDC software, as illustrated in Fig. 5.

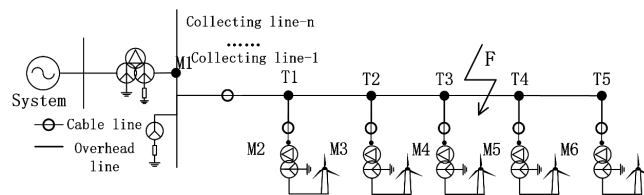


Fig. 5. Simplified model of wind farm collector lines

The wind turbine adopted high-precision distributed sensors (bandwidth 0.1 Hz-10 MHz); the apparatus was employed to capture the fault traveling wavehead signal; the collector line was linked to the 35 kV low-voltage side bus, with each line connected in series to five doubly-fed wind turbines., and a single machine was connected to the collector node through a 0.6 km cable with the adjacent turbines spaced at a distance of 1 km. The actual line parameters on site were strictly referenced to the design specification for wind farms [22]. The sensor noise model (e.g., Gaussian white noise) was introduced to simulate the actual working conditions.

More details can be found in Table 1.

**Table 1.** Simulation used to calculate the distribution parameters

Type of collector line	Component of each order	Resistance/ Ohm*km	Inductance/ $10^{-4}$ H/km	Capacitance/ $10^{-9}$ F/km
Cable line	Positive sequence	0.02672	9.036	2.773
	Zero sequence	0.3163	30.530	7.952
Overhead line	Positive sequence	0.01672	4.336	17.730
	Zero sequence	00.15163	2.530	5.952

PSCAD (4.6.3) software package was utilized for simulation [23], whereas Matlab (2021b) software was employed for data analysis and processing [24]. The sampling frequency was 1 MHz, the simulation time step was 1  $\mu$ s, and the equivalent propagating speed of the fault traveling wave in the hybrid line was derived via Eq. (21) as  $2.186 \times 10^5$  km/s. This study first validated the effectiveness of the proposed fault-ranging scheme and then assessed the effects of different noise disturbances, transition resistances, and initial phases on the experimental results.

#### 4.1 Precise Localization Based on Double-ended Traveling Waves

**Line failure between T-nodes.** The fault occurrence was set at 0.3 km of the nodal branch T3T4 near T3, the fault type was Ag, with an initial angle of  $10^\circ$ . The transition resistance was  $\Omega$ , and the total simulation duration was 0.02 s, comprising 0.002 s of steady-state operation prior to the fault and 0.018 s of transient response following the fault. The fault voltage traveling wave within 1-3.5 ms (including the time from the fault point to each endpoint) was collected for analysis, and the first fault voltage signal within this period is shown in Fig. 6.

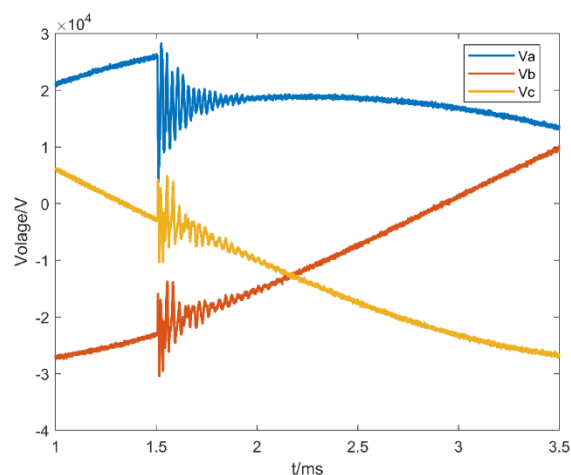


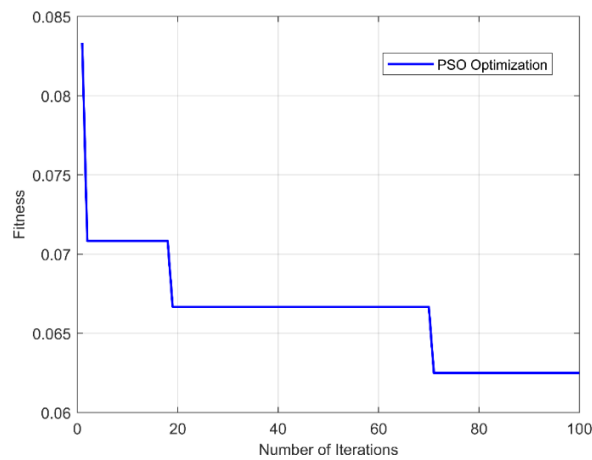
**Fig. 6.** Multi-branch collector line fault localization method

The observed defective traveling wave was converted via the Karenbauer phase mode transform to derive the fault signal's traveling wave line mode component  $U\alpha$ . The PSO optimization algorithm was employed to optimize the VMD dynamic parameters  $K$  and  $\alpha$ , with the parameter configurations for the PSO algorithm presented in Table 2.

**Table 2.** Simulation used to calculate the distribution parameters

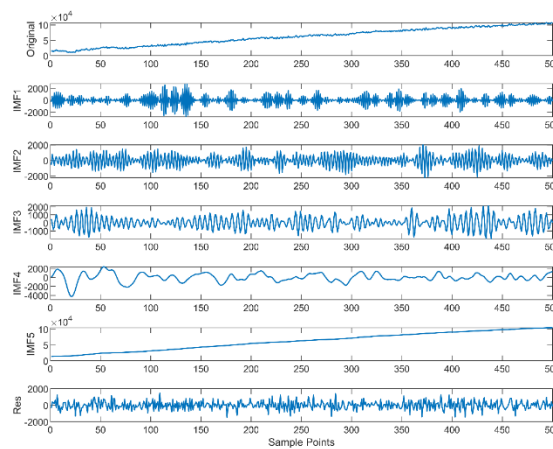
$G_{\max}$	M	$c_1$	$c_2$	$\omega$
30	100	2	2	1

Fig. 7 shows the variation curve of minimum envelope entropy of line mode components at line endpoints with the number of iterations during the parameter optimization process.



**Fig. 7.** Fitness curve of minimum envelope entropy versus the number of iterations

In this paper, the VMD parameters were optimized by PSO to attain the optimal dynamic parameters  $U_\alpha$ :  $K = 5$ ,  $\alpha = 634$  for decomposing the line mode signals. The signals were decomposed using the VMD, as illustrated in Fig. 8.



**Fig. 8.** VMD decomposition results

Finally, using the improved TEO energy calculation, each port's extracted instantaneous energy characteristics were derived and plotted in Fig. 9. The time the obtained fault traveling wave reached each endpoint was substituted into Eq. (13), and the distance of the fault to each endpoint was calculated and listed in Table 3.

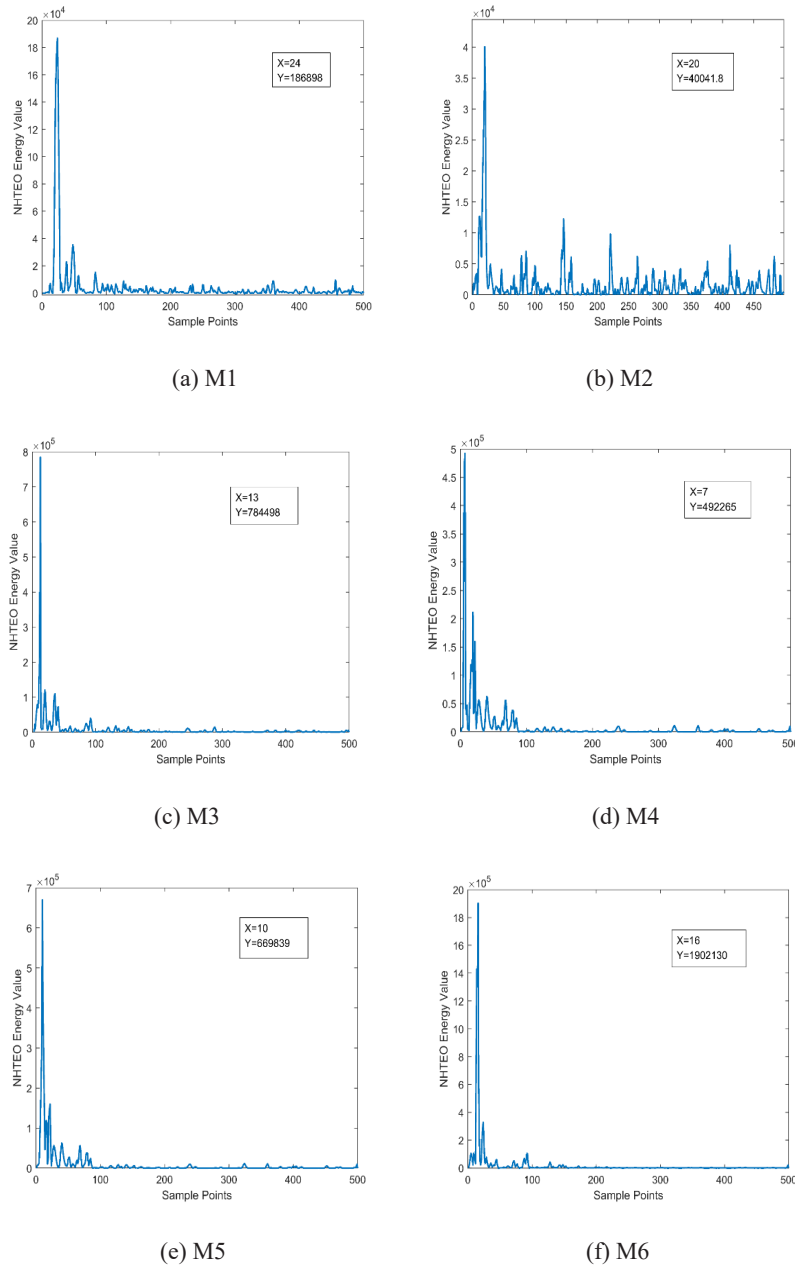


Fig. 9. Energy operator results for improved TEO at endpoints

Table 3. Fault distance calculation for each endpoint

Terminal	Wavefront arrival time		Fault distance
	(μs)		(km)
M1	24		3.479
M2	20		2.899
M3	13		1.885
M4	7		1.015
M5	10		1.450
M6	16		2.319

The fault distance difference matrix  $D$  was constructed based on the fault distance derived from Table 3. The intrinsic line distance difference matrix  $L$  was constructed from the original data to obtain the branch judgment matrix  $\delta$  via Eq. (22).

$$\delta = \begin{bmatrix} 0 & 0 & 2.194 & 4.064 & 4.629 & 4.167 \\ 0 & 0 & 2.014 & 3.884 & 3.449 & 4.507 \\ -2.194 & -2.014 & 0 & 1.870 & 2.112 & 2.590 \\ 0 & 0 & 0 & 0 & 0.492 & 0.691 \\ -4.629 & -3.449 & 0.279 & -0.565 & 0 & 1.382 \\ -4.760 & -4.580 & 0.197 & -0.696 & 0 & 0 \end{bmatrix}. \quad (22)$$

Since the  $\delta$  matrix satisfied the condition  $\delta(4, :)*\delta(:, 5) = 0$ , the fault was found to occur in the T3T4 segment, which was consistent with the actual fault segment.

The simulation findings indicate that a ground fault is present in section T3T4. The distance from the fault location and the ends of M4 and M5 was calculated using double-ended traveling wave fixing. It was concluded that the fault occurred at a distance of 0.281 km in the branch of the node T3T4 near the node of T3. The ranging error was -0.019 km, meeting the fault's precise localization requirements.

**WTG Branch Circuit Failures.** Similarly, the fault was set to occur at the node branch M3T2 at 0.3 km from T2, the fault type was Ag, the fault's initial angle was  $10^\circ$ , the transition resistance was  $1\Omega$ , and the total simulation time was 0.02 s. The results of the fault distances of each endpoint calculated by PSO-VMD-TEO are listed in Table 4.

**Table 4.** Fault distance calculation for each endpoint

Terminal	Wavefront arrival time ( $\mu\text{s}$ )	Fault distance (km)
M1	15	2.175
M2	13	1.885
M3	2.5	0.362
M4	13	1.885
M5	15	2.175
M6	25	3.624

The calculation results of Table 4 were incorporated into Eqs. (15) and (16) to construct the fault section discrimination matrix  $\delta'$  as follows:

$$\delta' = \begin{bmatrix} 0 & 0.290 & 1.543 & 0.290 & 0 & -1.449 \\ -0.290 & 0 & 1.529 & 0 & -0.29 & -1.739 \\ -1.543 & -1.523 & 0 & -1.523 & -1.813 & -3.262 \\ -0.290 & 0 & 1.523 & 0 & -0.29 & -1.739 \\ 0 & 0.290 & 1.813 & 0.29 & 0 & -1.449 \\ 1.449 & 1.739 & 3.262 & 1.739 & 1.449 & 0 \end{bmatrix}. \quad (23)$$

By analyzing the characteristics of the elements in the matrix  $\delta'$ , it was found that the values of the elements in the third row of the matrix were not less than 0, and the values of the elements in the third column did not exceed zero, satisfying both  $\delta(:, 3)_{\min} \geq 0$  and  $\delta(3, :)\max \leq 0$  conditions. Therefore, it was concluded that the fault occurred in the branch of M3T2, coinciding with the actual fault zone.

The above fault section was M3T2. Using double-ended traveling wave fixing to calculate the distance between the fault point and the M3 and M4 ends, it was concluded that the fault occurred in the M3T2 node branch

close to the M3 endpoint at 0.311 km, and the ranging error was 0.011 km, which satisfied the fault's precise localization.

#### 4.2 Precise Localization Based on Double-ended Traveling Waves

The simulation evaluated various fault types to validate the method's feasibility. Eleven fault types were simulated for eleven sets of twenty fault cases each, encompassing  $A_g$ ,  $B_g$ ,  $C_g$ ,  $AB_g$ ,  $AC_g$ ,  $BC_g$ ,  $AB$ ,  $AC$ ,  $BC$ ,  $ABC_g$ . The above fault categories were established in the T4T5 line segment, located 0.4 km from the T4 node. Table 5 provides the results and actual fault distances for this segment.

**Table 5.** Comparative experiments with different fault types

Fault type	Criteria met or not	Identified section	Ranging error (km)
$A_g$	Yes	T4T5	0.014
$B_g$	Yes	T4T5	0.016
$C_g$	Yes	T4T5	0.008
$AB_g$	Yes	T4T5	0.024
$AC_g$	Yes	T4T5	0.016
$BC_g$	Yes	T4T5	0.018
$AB$	Yes	T4T5	0.024
$AC$	Yes	T4T5	0.015
$BC$	Yes	T4T5	0.031
$ABC_g$	Yes	T4T5	0.017

Table 5 shows that the results were independent of fault type, and the minimum measurement error was less than 50 m in 20 simulations.

#### 4.3 Effect of Transition Resistance

During the operation of wind farms, more non-metallic ground faults occur. Therefore, in the collector line branch near the node of the T2M3 branch, 0.2 km from the T2 node to set  $A_g$  and  $AB_g$  faults, the transition resistances were set at 0.01, 5, 10, 20, and 50  $\Omega$ . The algorithm of this paper is used for zone positioning and fault ranging, and the results of the zones are given in Table 6, along with the distance of the actual faults.

**Table 6.** Fault distance calculation for each endpoint

Fault type	Transition resistance ( $\Omega$ )	Criteria met or not	Identified section	Ranging error (km)
$A_g$	0.01	Yes	T2M3	0.013
	5	Yes	T2M3	0.027
	10	Yes	T2M3	0.046
	20	Yes	T2M3	0.053
	50	Yes	T2M3	0.078
$AB_g$	0.01	Yes	T2M3	0.018
	5	Yes	T2M3	0.026
	10	Yes	T2M3	0.026
	20	Yes	T2M3	0.049
	50	Yes	T2M3	0.067

From the above table, it can be concluded that the method proposed in this paper is less affected by the transition resistance, and the measurement errors are all less than 100 m in the occurrence of ground faults via 50  $\Omega$  transition resistance.

#### 4.4 Effects of Noise Interference

The collected data will have noise in actual operation, affected by the environment or line operation mode. To validate the anti-interference capability of the technology provided in this research and to assess the applicability of the wavehead extraction technique in a noisy backdrop, various signal-to-noise ratios (SNR) were incorporated into the acquired traveling wave signal, as illustrated in Fig. 10. Gaussian white noises with signal-to-noise ratios of 80, 40, and 20 dB were superimposed on the defective traveling wave signals obtained at each endpoint, respectively. The fault was set to manifest in the T3T4 interval segment, located 0.6 km from the T3 node, and is classified as a single-phase ground fault.

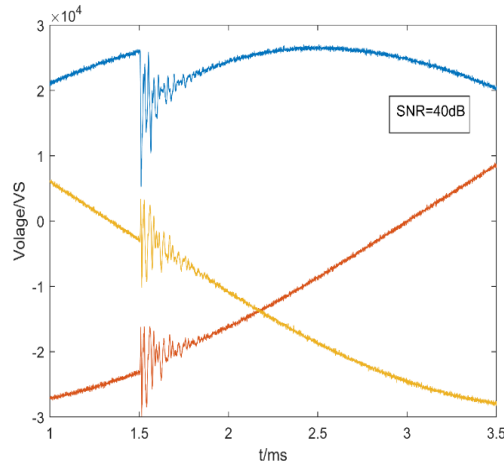


Fig. 10. Superposition of the voltage at the M1 end with SNR=40dB noise

The VMD parameters after PSO optimization were as follows:  $K=10$  and  $\alpha=719$  at SNR=80dB;  $K=10$  and  $\alpha=1773$  at SNR=40dB;  $K=5$  and  $\alpha=2698$  at SNR=20dB. Based on the fault localization results in Table 7, it was concluded that the optimal  $K$  and  $\alpha$  values in the VMD were determined after PSO optimization search, effectively locating the faults under different noise disturbances.

Table 7. Fault distance calculation for each endpoint

Noise Level (dB)	Criteria met or not	Identified section	Ranging error (km)
80	Yes	T3T4	-0.027
40	Yes	T3T4	0.045
20	Yes	T3T4	0.112

#### 4.5 Impact of Wavehead Detection Methods

To demonstrate the benefits of the fault wavehead detection method introduced in this paper, EMD-TEO, CCEMD-TEO, VMD-TEO, and the proposed method were employed for fault localization of collector lines. The fault was assumed to occur in the T3T4 interval, 0.6 km from the T3 node, and was classified as a single-phase ground fault. Table 8 displays the range results of four distinct approaches under various fault conditions.

Table 8. Localization results of different decomposition methods under noise interference

Decomposition method	Noise (dB)	Criteria met	Identified section	Ranging error (km)	Relative error
EMD-TEO	80	Yes	T3T4	0.147	6.363%
	40	No	-	-	-
	20	No	-	-	-

CCEMD-TEO	80	Yes	T3T4	0.027	1.227%
	40	No	-	-	-
	20	No	-	-	-
VMD-TEO	80	Yes	T3T4	0.027	1.227%
	40	Yes	T3T4	0.167	7.590%
	20	No	-	-	-
The proposed method	80	Yes	T3T4	-0.024	1.090%
	40	Yes	T3T4	0.045	2.045%
	20	Yes	T3T4	0.112	5.091%

To characterize the discrepancy in the ranging findings of various approaches, the relative error  $\varepsilon$  was defined to quantify the difference between the measured value  $x$  and the true value  $x'$ , with the calculation formula provided as follows:

$$\varepsilon = \frac{|x - x'|}{L} \times 100\% \quad (24)$$

Table 8 demonstrates that the proposed method surpasses EMD-TEO, CCEMD-TEO, and VMD-TEO in mitigating noise interference and satisfies the practical engineering requirements of wind farm collector lines.

## 5 Conclusions

To mitigate the difficulty of wind farm collector line fault localization, this paper proposed a PSO-VMD-TEO-based fault traveling wave detection method and a multi-branch collector line fault localization method.

(1) Based on the minimum envelope entropy fitness function, the PSO algorithm dynamically optimized the VMD parameter  $K$  and the penalty factor  $\alpha$ , effectively suppressing noise and harmonic interference. Combined with the improved TEO energy arithmetic, it ensured the high-precision detection of the traveling wavehead under an environment with a signal-to-noise ratio as low as 20 dB.

(2) By constructing the difference discriminant matrix between the intrinsic distance matrix and the fault distance matrix, we eliminated the dependence on the zero-sequence component. Now, it can be applied to the section localization of all fault types, such as three-phase short circuits.

(3) Through the hybrid line equivalent wave speed normalization and error tolerance correction, the double-ended traveling wave ranging method was applied, featuring has a ranging error of less than 100 m in many scenarios, and the maximum relative error did not exceed 5.1%. The method significantly outperformed the conventional EMD-TEO, CCEMD-TEO, and VMD-TEO schemes regarding noise immunity and transition resistance adaptation.

## Acknowledgement

This study was financially supported by the Science and Technology Development Plan Project of Jilin Province of China (grant No. 20240402059GH).

## References

- [1] P. Lakshmanan, R. Sun, J. Liang, Electrical collection systems for offshore wind farms: A review, *CSEE Journal of Power and Energy Systems* 7(5)(2021) 1078-1092. <https://doi.org/10.17775/CSEEJPES.2020.05050>
- [2] M. He, W. Jiang, W. Gu, TriChronoNet: Advancing electricity price prediction with Multi-module fusion, *Applied Energy* 371(2024) 123626. <https://doi.org/10.1016/j.apenergy.2024.123626>

- [3] W. Liu, Analysis and treatment of faults in collecting lines of coastal mountain wind farms, *Automation Application* (2) (2021) 91-93.  
<https://doi.org/10.19769/j.zdhy.2021.02.028>
- [4] L. Li, T. Sun, S. Zeng, L. Wang, J. Liang, Y. Hao, Fault location method for distribution networks based on traveling wave time difference, *Power System Protection and Control* 50(3)(2022) 140-147.  
<https://doi.org/10.19783/j.cnki.pspc.210003>
- [5] H. Shu, X. Liu, X. Tian, Single-ended fault location for hybrid feeders based on characteristic distribution of traveling wave along a line, *IEEE Transactions on Power Delivery* 36(1)(2021) 339-350.  
<https://doi.org/10.1109/TPWRD.2020.2976691>
- [6] D. Guillen, C. Salas, L. F. Sanchez-Gomez, L. M. Castro, Enhancement of dynamic phasor estimation-based fault location algorithms for AC transmission lines, *IET Generation, Transmission & Distribution* 14(6)(2020) 1091-1103.  
<https://doi.org/10.1049/iet-gtd.2019.0051>
- [7] M. Fayazi, M. Joorabian, A. Saffarian, M. Monadi, A single-ended traveling wave based fault location method using DWT in hybrid parallel HVAC/HVDC overhead transmission lines on the same tower, *Electric Power Systems Research* 220(2023) 109302.  
<https://doi.org/10.1016/j.epsr.2023.109302>
- [8] H. Wang, D. Yang, B. Zhou, X. Gao, Y. Pang, Fault diagnosis of multi-terminal HVDC transmission line based on parallel convolutional neural network, *Automation of Electric Power Systems* 44(12)(2020) 84-92.  
<https://doi.org/10.7500/AEPS20191124003>
- [9] J. Chen, E. Chu, Y. Li, B. Yun, H. Dang, Y. Yang, Faulty feeder identification and fault area localization in resonant grounding system based on wavelet packet and Bayesian classifier, *Journal of Modern Power Systems and Clean Energy* 8(4)(2020) 760-767.  
<https://doi.org/10.35833/MPCE.2019.000051>
- [10] Y. Li, T. Zheng, A. Wen, Research on single-phase grounding fault location method for EHV AC transmission lines based on single-ended quantities, *Power System Protection and Control* 48(6)(2020) 27-33.  
<https://doi.org/10.19783/j.cnki.pspc.190555>
- [11] Z. Y. Cheng, X. J. Li, M. J. Tang, S. Xia, Single terminal fault location method based on fault current distribution factor, *Electrical Measurement and Instrumentation* 55(1)(2018) 126-130.  
<https://doi.org/CNKI:SUN:DCYQ.0.2018-01-021>
- [12] L. Li, T. Sun, S. Zeng, L. Wang, J. Liang, Y. Hao, Fault location method for distribution networks based on traveling wave time difference, *Power System Protection and Control* 50(3)(2022) 140-147.  
<https://doi.org/10.19783/j.cnki.pspc.210003>
- [13] C. Zhang, G. Song, T. Wang, L. Yang, Single-ended traveling wave fault location method in DC transmission line based on wave front information, *IEEE Transactions on Power Delivery* 34(5)(2019) 2028-2038.  
<https://doi.org/10.1109/TPWRD.2019.2922654>
- [14] A.P. Oliveira, F.A. Moreira, A.F. Picanço, Accuracy analysis using the EMD and VMD for two-terminal transmission line fault location based on traveling wave theory, *Electric Power Systems Research* 224(2023) 109667.  
<https://doi.org/10.1016/j.epsr.2023.109667>
- [15] L. Xie, Y. Li, L. Luo, X. Zeng, Y. Cao, Fault location method for multi-branch lines based on extreme-point symmetric mode decomposition, *Proceedings of the CSEE* 41(21)(2021) 7326-7338.  
<https://doi.org/10.13334/j.0258-8013.pcsee.201320>
- [16] J. Wu, G. Qiu, C. Wu, W. Jiang, J. Jin, Federated learning for network attack detection using attention-based graph neural networks, *Scientific Reports* 14 (2024) 19088.  
<https://doi.org/10.1038/s41598-024-70032-2>
- [17] Y. Lu, W. Wang, R. Bai, S. Zhou, L. Garg, A. K. Bashir, W. Jiang, X. Hu, Hyper-relational interaction modeling in multi-modal trajectory prediction for intelligent connected vehicles in smart cities, *Information Fusion* 114(2025) 102682.  
<https://doi.org/10.1016/j.inffus.2024.102682>
- [18] X. Wang, F. Zhang, J. Gao, L. Guo, X. Wang, Z. Liang, W. Liu, Fault location based on variable mode decomposition and kurtosis calibration in distribution networks, *International Journal of Electrical Power & Energy Systems* 154(2023) 109463.  
<https://doi.org/10.1016/j.ijepes.2023.109463>
- [19] B. Yang, X. Wang, Y. Xing, C. Cheng, W. Jiang, Q. Feng, Modality fusion vision transformer for hyperspectral and LiDAR data collaborative classification, *IEEE Journal of Selected Topics in Applied Earth Observations and Remote Sensing* 17 (2024) 17052 -17065.  
<https://doi.org/10.1109/JSTARS.2024.3415729>
- [20] H. Peng, W. Wang, Y. Zhu, H. Gao, R. Li, Intelligent single-phase grounding fault location for wind farm collection line based on LSTM neural network, *Power System Protection and Control* 49(16)(2021) 60-66.  
<https://doi.org/10.19783/j.cnki.pspc.201457>
- [21] Z. Meng, W. Du, H. Wang, Distribution Network Fault Area Location Based on Deep Convolution Neural Network with Transfer Learning, *Southern Power Grid Technology* 13(7)(2019) 25-33.  
<https://doi.org/10.13648/j.cnki.issn1674-0629>

- [22] Ministry of Housing and Urban-Rural Development, People's Republic of China, Code for design of wind farm: GB 51096-2015, China Planning Press, 2015.
- [23] Manitoba HVDC Research Centre, PSCAD (Version 4.6.3), [Computer software], Winnipeg, MB, Canada, 2021.
- [24] The MathWorks Inc., MATLAB, Version 9.11 (R2021b), Natick, Massachusetts, 2021.